Improved Weldability for Laser Welding Press-Hardened Steel via Thinning Coatings: Part 1 — Microstructure Characterization and Mechanical Testing

Laser welding of press-hardened steels with thinner coatings exhibited better weldability due to a lower volume fraction of ferrite in the welds

BY Z. Q. JIN, S. GUO, Z. Y. ZHANG, Y. Q. WANG, Z. X. LI, H. L. YI, AND G. M. XIE

Abstract

As integrated door rings with high safety are being used for automotive applications, Al-Si-coated press-hardened steel (PHS) is attracting wider attention. However, during laser welding of thickly coated (~30 μm) PHS, excessive ferrite is formed in the weld, so it is necessary to use a filler metal to limit this issue. This work investigated the laser weldability of thinly (~16 μm) and extra-thinly (~10 μm) coated PHSs using a low-cost C-Mn filler wire at weld travel speeds of 3–7 m/min. The results indicated that laser welding of PHSs with thinner coatings exhibited better weldability due to a lower-volume fraction of ferrite in the weld. However, the thinly coated PHS joint welded at 7 m/min failed at the Al-enriched weld toe, where strip-like ferrite was observed. Al enrichment originated from the coating outside the weld, and the extent of Al enrichment was closely related to the high welding speed.

Keywords

- Press-Hardened Steel
- Al-Si Coating
- Laser Tailor Welding
- Weldability

https://doi.org/10.29391/2025.104.015

Introduction

To meet the demands of light weight and safety in automobiles, integrated door rings consisting of Al-Si-coated press-hardened steel (PHS) are widely used in automobile bodies (Refs. 1–3). Laser tailor welding of various PHS blanks is a crucial step in producing door rings (Ref. 4). However, during laser welding, the Al element in the coating typically enters the weld, leading to the formation of soft ferrite and deteriorating the mechanical properties of the welded joints (Refs. 5–8).

In the last decade, some studies focused on improving the mechanical properties of the PHS joints. High-frequency pulsed laser ablation was carried out to remove the coating before laser welding, which could prevent Al from entering the weld. However, the laser ablation process was inefficient and was accompanied by Al vapor contamination (Ref. 9). When a pulsed or oscillating laser beam was employed to stir the molten pool more violently, a more-uniform distribution of Al was achieved in the weld without changes to the martensite fraction (Refs. 10, 11). Despite these improvements, the weld was still a weak region, and the maximum achievable welding speed to avoid ferrite was relatively low (~3 m/min). Furthermore, the filler materials containing austenite stabilizing elements, such as the Ni material (Ni content ≥ 10 wt-%), were widely applied to inhibit the formation of ferrite during laser welding of Al-Si-coated PHS (Refs. 12–17). Although these materials improved the mechanical properties of the Al-Si-coated PHS joints, they were expensive, and their acceptable dilution levels were limited to a narrow range.

Recently, Yi et al. found that using a thinner Al-Si coating could enhance the bending toughness of PHS by reducing the

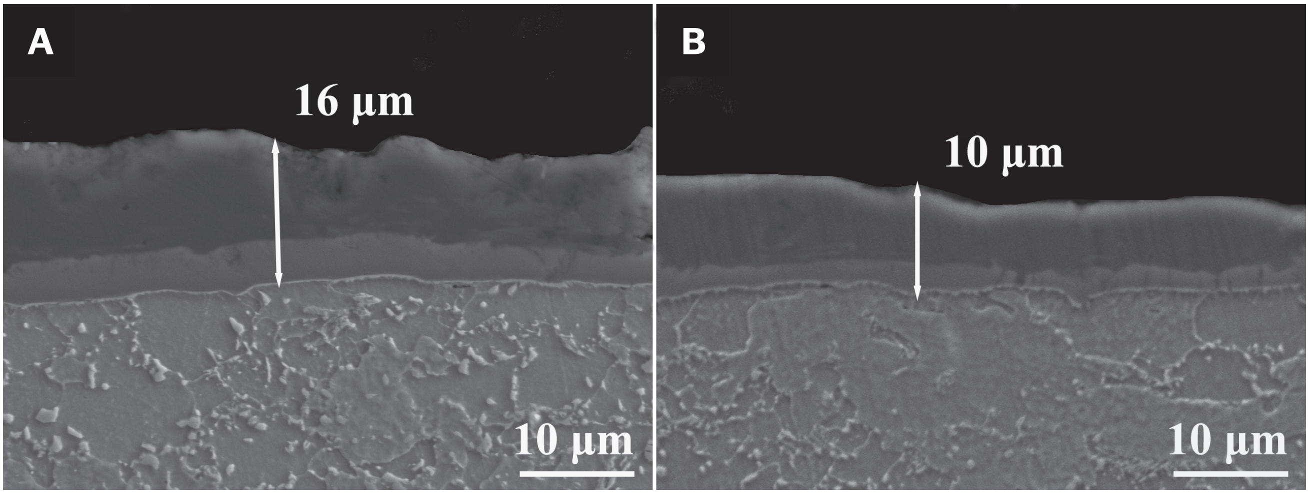

Fig. 1 — Optical microscope (OM) images of PHS: A — Thin coating; B — extra-thin coating.

Table 1 — Chemical Compositions of the PHS, Al-Si Coating, and Filler Wire (wt-%)

Materials	C	Mn	Al	Si	Ni	Cr	B	P	S	Fe
PHS	0.23	1.18	0.034	0.22	—	0.16	0.0025	0.025	0.001	Bal.
Al-Si Coating	—	—	90.00	8.00	—	—	—	—	—	2.00
C-Mn Wire	0.30	0.50	—	—	—	—	—	0.03	0.0015	Bal.

C enrichment at the interface between the coating and steel substrate (Refs. 18, 19). Given the reduction of Al content in thin coatings, it was assumed that the weldability of the Al-Si-coated PHS would improve. Sound weldability implied a wide welding window with limited filler wire addition during laser welding of PHS, which was important for enhanced efficiency, decreased costs, and improved industrial production quality.

In this work, coating thickness was decreased from the conventional 25–35 µm to 13–18 µm (thin coating) and 8–13 µm (extra-thin coating). The PHS with thin and extra-thin coatings were laser welded using a C-Mn wire at a wide welding speed range of 3–7 m/min. The welded joints' metallurgical behavior and mechanical properties were studied in detail.

Experimental Procedure

This work utilized thinly coated (~16 µm) and extra-thinly coated (~10 µm) PHS plates with 1.2 mm thickness. The optical microscope (OM) images of the coatings, composed of Al-Si alloy, are shown in Fig. 1. Another phase, likely an intermetallic compound, apparently was formed at the interface between the coating and steel substrate, given the different contrast in the micrograph. The chemical compositions of the PHS and the Al-Si coating are listed in Table 1.

Figures 2A and B show the laser-filler wire welding process. The laser welding system consisted of an RFL-C 6000 fiber laser, a KUKA robot, and a RayTools BW240 welding head. A Fronius CMT wire feeder was used to feed the wire. A C-Mn wire with a 1.0 mm diameter was used; its composition is shown in Table 1. During the welding process, the wire was located at the front of the laser beam, and the feeding angle was 60 deg from the horizontal direction. Pure argon was used as a shielding gas at a flow rate of 20 L/min. The diameter of the shielding gas nozzle was 10 mm, the blowing angle was 45 deg from the horizontal direction, and the distance between the nozzle and the weld surface was 5 mm. Detailed welding parameters are listed in Table 2. The surface focusing position of the laser was 300 mm above the steel surface, and the defocus of –5mm meant that the welding head was moved down 5 mm from the surface focusing position. The wire volume added per unit length of weld (V_w/unit L) was quantitated using the following equation (assuming 100% capture efficiency):

$$V_w/\text{unit L} = \frac{L_f \pi r^2}{L_t} = \frac{v_f T_f \pi r^2}{v_t T_t} \tag{1}$$

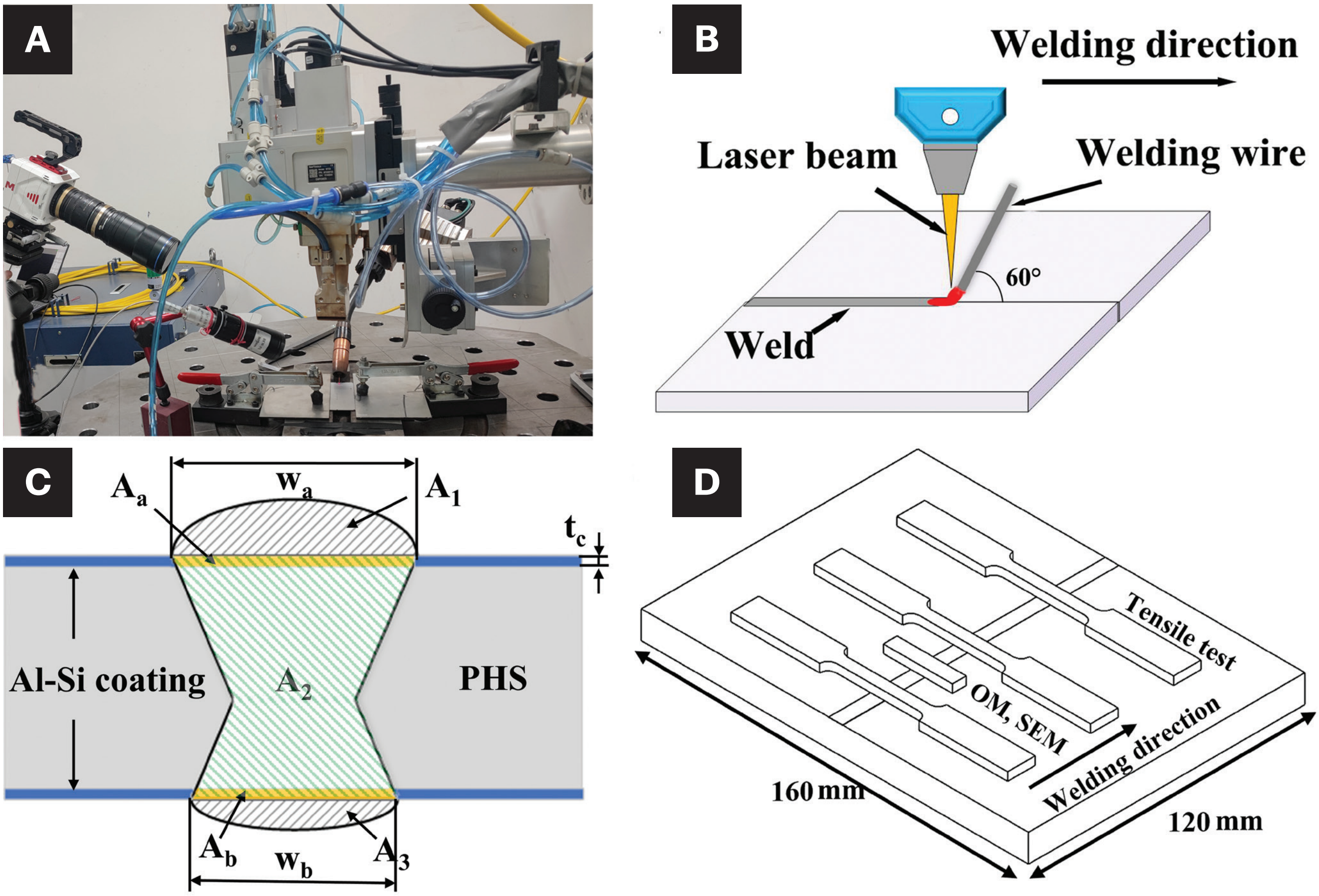

Fig. 2 — A and B — Laser–filler wire welding process; C — schematic diagram depicting the calculation of the dilution rate; D — sampling positions of the microstructural and tensile samples.

Table 2 — Welding Parameters for Laser-Filler Wire Welding of Al-Si-Coating PHS

Welding Speed (v_t)/m/min	Laser Power/kW	Heat Input (Q)/ kJ/cm	Wire Feeding Rate (v_f)/m/min	Wire Volume per Unit Length (V_w)/ m^3/m	Defocusing Distance (L)/mm
3	2.5	0.50	1.2	3.14×10^{-6}	–5
5	4.0	0.48	1.2	1.88×10^{-6}	–5
7	5.0	0.43	1.2	1.35×10^{-6}	–5

where Lf is the wire feeding length (m), Lt is the weld length (m), vf is the wire feeding rate (m/min), vt is the welding speed (m/min), r is the wire radius (m), Tf is the wire feeding time (min), and Tt is the welding time (min). Additionally, the same values of T_f and T_t were used for each trial.

A high-speed camera (Revealer M220M, China) was used to monitor the dynamic behaviors of the molten pool at 2000 frames per second (fps), as shown in Fig. 2A. After welding, the tailor-welded blanks were heated to 920°C, held for 5 min, and then press-hardened at a cooling rate of 60°C/s, which promoted a martensite microstructure with an ultimate tensile strength of above 1500 MPa.

The weld dilution rate was calculated using the following equation:

$$D = \frac{A_2}{A_1 + A_2 + A_3} \tag{2}$$

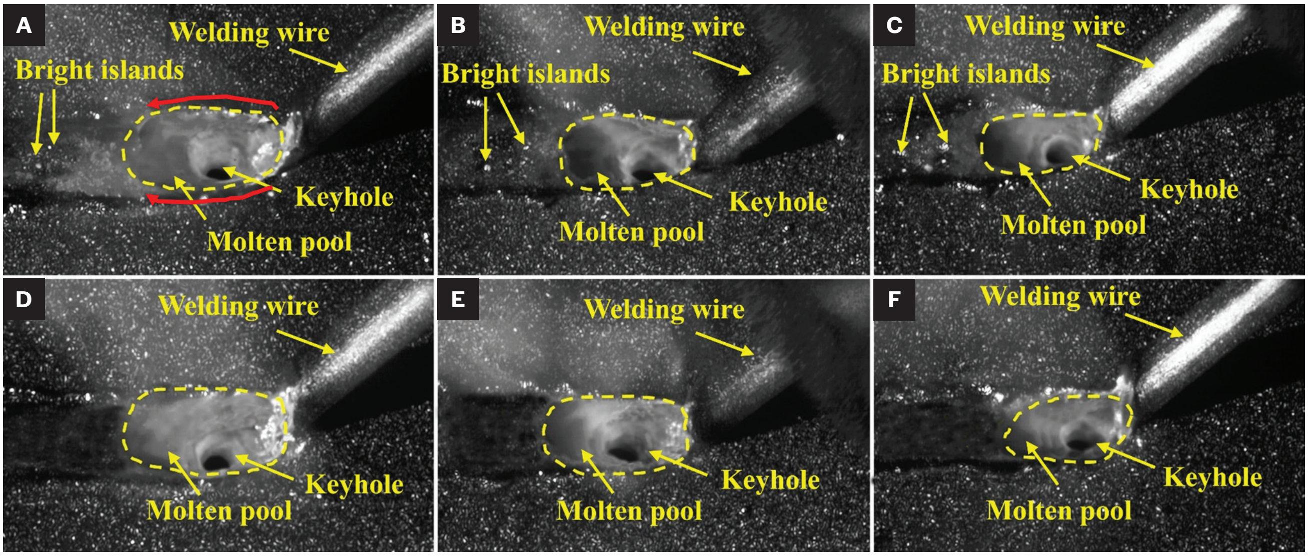

Fig. 3 — Dynamic behaviors of the molten pools: A–C — Thinly coated PHS; D–F — extra-thinly coated PHS; A and D — 3 m/min; B and E — 5 m/min; C and F — 7 m/min.

where D is the dilution rate and A_1, A_2, and A_3 are the areas of top reinforcement, resolidified base metal (BM), and root reinforcement. Additionally, A_2 contained the areas of coating on the top and bottom surfaces of the PHS (A_a and A_b), as shown in Fig. 2C. This value of D indicated the ratio of BM and coating in the fusion zone, which was closely related to the filler wire addition.

The element contents (except Al and Si) of the weld were obtained according to the following formula:

$$\mathrm{W} = \mathrm{D} \times Wa + (1\text{-D}) \times Wb \tag{3}$$

where W, Wa, and Wb are the wt-% contents of the weld, PHS, and filler wire, respectively. Additionally, the equation for calculating the Al content of the weld was estimated as:

$$\begin{aligned} W_{Al} &= \frac{(A_a + A_b)\eta}{A_1 + A_2 + A_3} \times \frac{\rho_{Al}}{\rho_{Fe}} \\ &= \frac{(w_a + w_b)t_c\eta}{A_1 + A_2 + A_3} \times \frac{\rho_{Al}}{\rho_{Fe}} \end{aligned} \tag{4}$$

where W_{Al} is the estimated Al content in the weld, A_a and A_b are the areas of molten coating on the top and bottom surfaces of the PHS, w_a and w_b are the width of molten coating on the top and bottom surfaces of PHS, t_c is the coating thickness, η is the proportion of Al in the coating (0.9), ρ_{Al} is the density of Al (2.7 g/cm^3), and ρ_{Fe} is the density of steel (7.8 g/cm^3). Continuous cooling transformation curves of the welds were simulated for the press-hardening heat treatment for each sample with different dilution levels using JMatPro® software. The initial temperature and cooling rate were set to 920°C and 60°C/s, respectively.

After press-hardening, the microstructural and tensile specimens of the joints were machined perpendicular to the welding direction (Fig. 2D). The microstructure was characterized by the Olympus DSX500 optical microscope (OM), Zeiss Ultra-55 scanning electron microscope (SEM), and FEI Tecnai G2 F20 transmission electron microscope (TEM). The element contents and distributions in the welds were analyzed by a JEOL-8530F electron probe microanalyzer (EPMA). Furthermore, the element content was the average value of 30 points in each weld. The OM, SEM, and EPMA specimens were mechanically polished and etched using a 4% nital solution for 10 s. Based on the different gray scales of the etched martensite and ferrite in the SEM images, the ferrite fraction was measured using Image-Pro Plus software with 10 SEM images. The transmission electron microscopy (TEM) specimens were electropolished with a 90% ethanol solution and 10% perchloric acid at –30°C. The Vickers hardness of the joints was measured using an FM-700 machine; the load was 300 gf, and the holding time was 10 s. To generate a hardness distribution map of the joints, 300 hardness indents were made in the BM and weld. Tensile tests were performed at an initial strain rate of 1.0×10^{-3} s^{-1} using a GOTECH AI-7000 tensile machine at room temperature. At least three samples were tested for each condition.

Results and Discussion

Metallurgical Behavior of the PHS Welds After Thinning the Coating

Figure 3 shows the dynamic behaviors of the molten pools during laser-filler wire welding under various conditions. An elliptical molten pool was formed, and the filler wire was fed into the molten pool depending on a liquid bridge transition. The formation of the keyhole indicated that it was penetration welding. During laser welding, the Al-Si

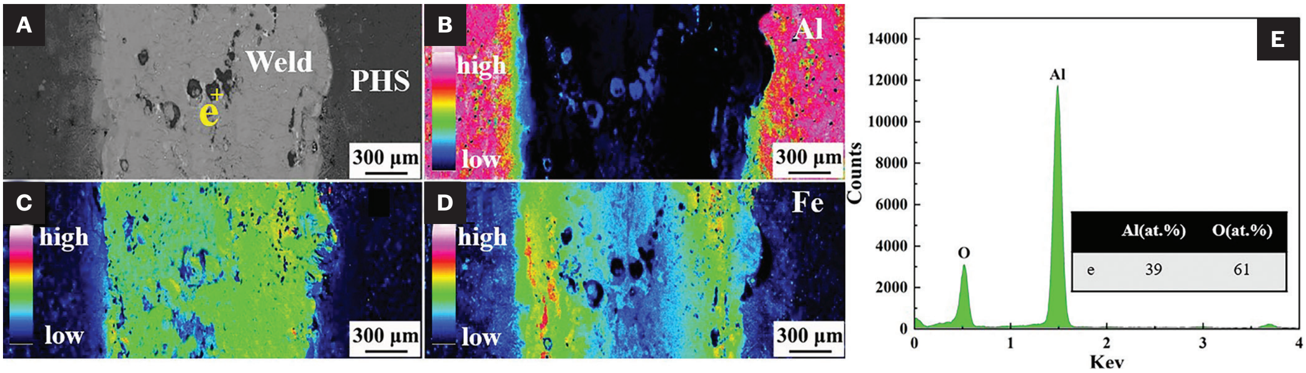

Fig. 4 — A — Backscattered electron image; B–D — EPMA elements map scan of the weld surface; E — EPMA point analysis of the black block on the weld surface.

Table 3 — The Dilution Rates and Ferrite Fractions of the Welds at Different Conditions

No.	Dilution Rate %	Ferrite Fraction %
Thin Coating (3 m/min)	78.4	1.5
Thin Coating (5 m/min)	83.4	2
Thin Coating (7 m/min)	86.9	3
Extra-thin coating (3 m/min)	79.4	—
Extra-thin coating (5 m/min)	82.2	—
Extra-thin coating (7 m/min)	85.5	—

coating melted. Part of the molten coating flowed backward from both sides of the keyhole, as shown by red arrows in Fig. 3A, and most of the coating flowed downward into the molten pool caused by the circulating flow. As the welding progressed, the coating flowing backward from both sides of the keyhole and the coating floating upward from the molten pool converged at the end of the molten pool, forming bright islands of a solid phase. Figure 4 illustrates the EPMA results of the weld surface after solidification. The black blocks of the weld surface in Fig. 4A corresponded to the bright islands on the molten pool surface, which was primarily comprised of Al and O elements, tentatively identified as Al_2O_3 via EPMA point analysis. Previously, Chen et al. observed the dynamic behaviors of the molten pools of PHSs with and without Al-Si coating. An Al_2O_3 film was formed on the weld surface of a coated PHS but not on the surface of an uncoated PHS (Ref. 20). Furthermore, at the higher welding speeds in the current study, the total area of bright islands observed on the molten pool surface of thinly coated PHS increased (Figs. 3A–C). As the welding speed increased, the heat input of laser welding decreased, leading to a smaller width and length of the molten pool, which decreased the dilution effect. In addition, the time for convective mixing was shorter at a higher welding speed due to the shorter residence time in the liquid. Therefore, the molten coating could not be diluted effectively, causing more coatings to converge on the molten pool surface, forming bright islands. In contrast, the bright islands on the molten pool surface of the extra-thinly coated PHS significantly decreased due to the reduced volume of the molten coating (Figs. 3D–F). For the traditional thickly coated PHS, previous research indicated that the area of the bright islands of the molten pool surface at a low welding speed of 3 m/min was larger depending on the thicker coating (Ref. 17).

Figure 5 shows the OM images of the thinly and extra-thinly coated PHS joints at welding speeds of 3–7 m/min. The fusion zones of all welds were X-shaped, with the reinforcement area maintained below 20% of the sheet's thickness according to the standard BS EN 10359:2023, *Laser welded tailored blanks - Technical delivery conditions*. Table 3 presents the weld dilution rates under various conditions. As the welding speed increased from 3 to 7 m/min, the dilution rates of the thinly coated PHS welds increased from 78.4% to 86.9%, while for extra-thinly coated PHS welds, it increased from 79.4% to 85.5%. The width of the welds gradually decreased with increasing welding speeds due to the reduction in heat input. At a constant wire feeding rate, the filler wire fraction decreased with increasing welding speeds. Thus, as the welding speed increased, a higher dilution rate was obtained depending on the reductions in filler wire fraction.

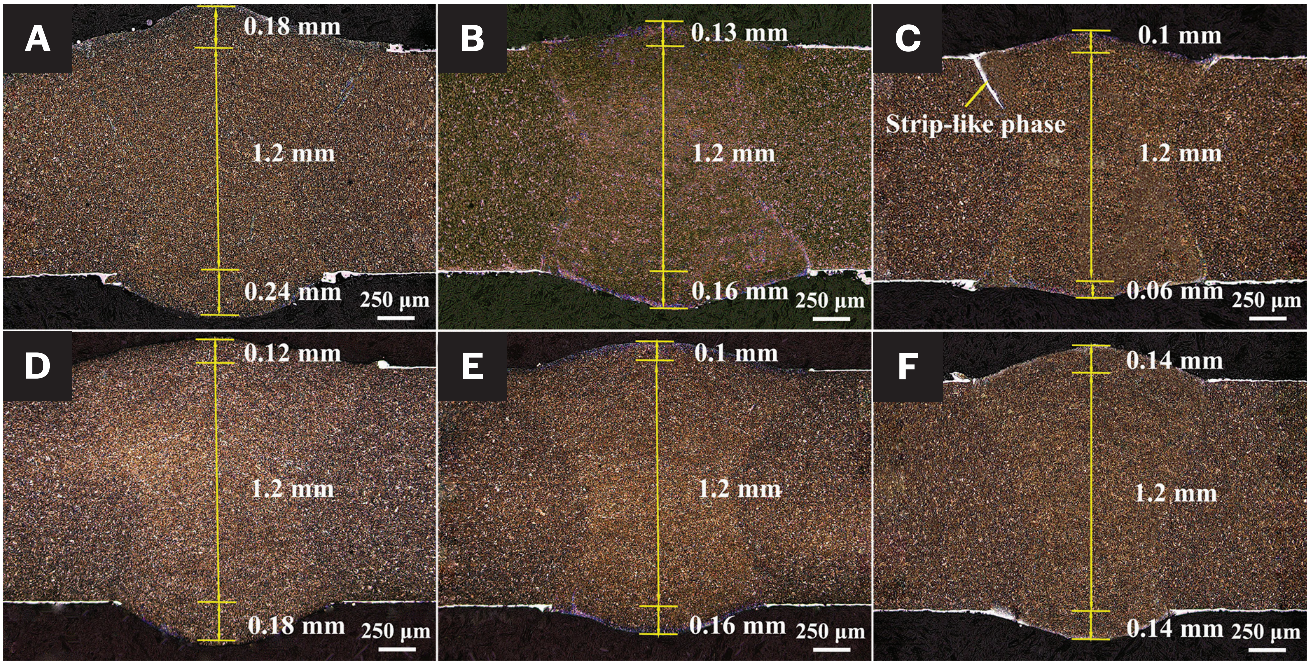

Fig. 5 — OM images of the thinly and extra-thinly coated PHS joints at different welding speeds: A–C — Thinly coated PHS; D–F — extra-thinly coated PHS; A and D — 3 m/min; B and E — 5 m/min; C and F — 7 m/min.

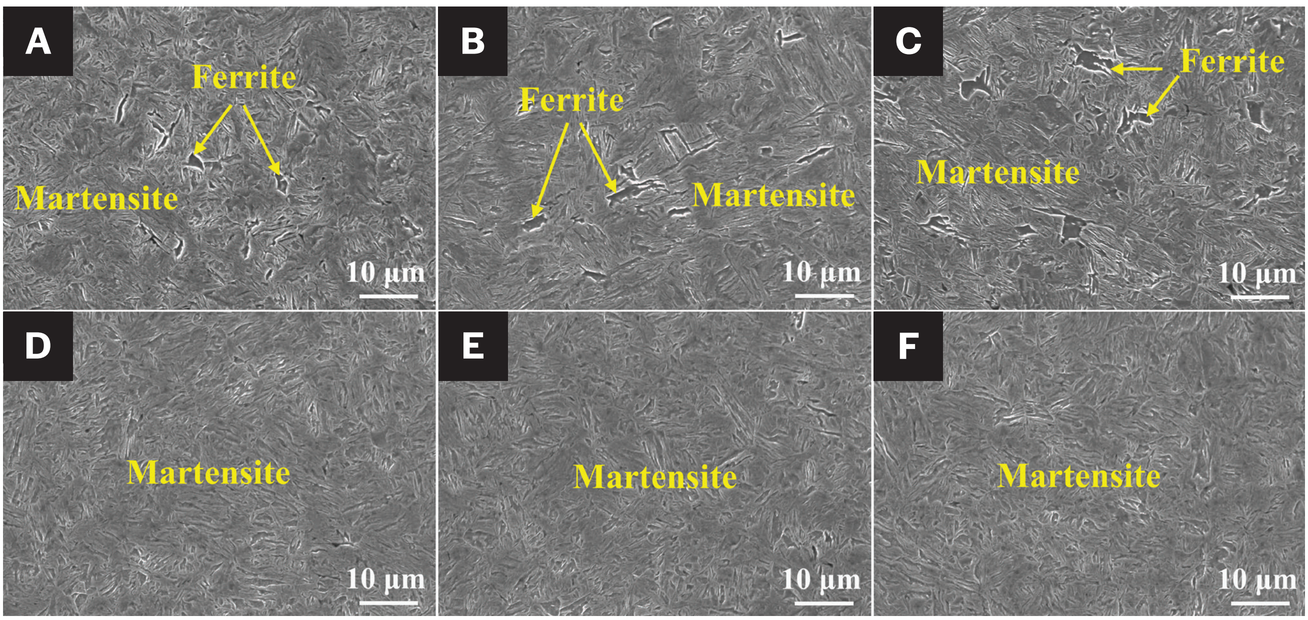

Fig. 6 — Scanning electron microscope (SEM) images of the thinly and extra-thinly coated PHS welds at different welding speeds: A–C — thin coating PHS; D–F — extra-thin coating PHS; A and D — 3 m/min; B and E — 5 m/min; C and F — 7 m/min.

The microstructures of welds of thinly coated PHS were uniform when the welding speeds were 3 and 5 m/min. However, a strip-like phase appeared for the thinly coated PHS near the weld toe obtained at a welding speed of 7 m/min (Fig. 5C). By comparison, at welding speeds of 3–7 m/min, no strip-like phase along the fusion boundary was observed with the extra-thinly coated PHS welds. This observation indicated that the welds without a noticeable strip-like phase could be achieved at a wider welding speed range after reducing the coating thickness, with a high dilution rate of > 78%. Previous reports noted that uniform welds were only obtained in the traditional thickly coated PHS at a relatively low dilution rate of 70% (Ref. 21).

Figure 6 shows the SEM images of the welds at different conditions. The microstructure of the thinly coated PHS welds, obtained at different welding speeds, consisted of

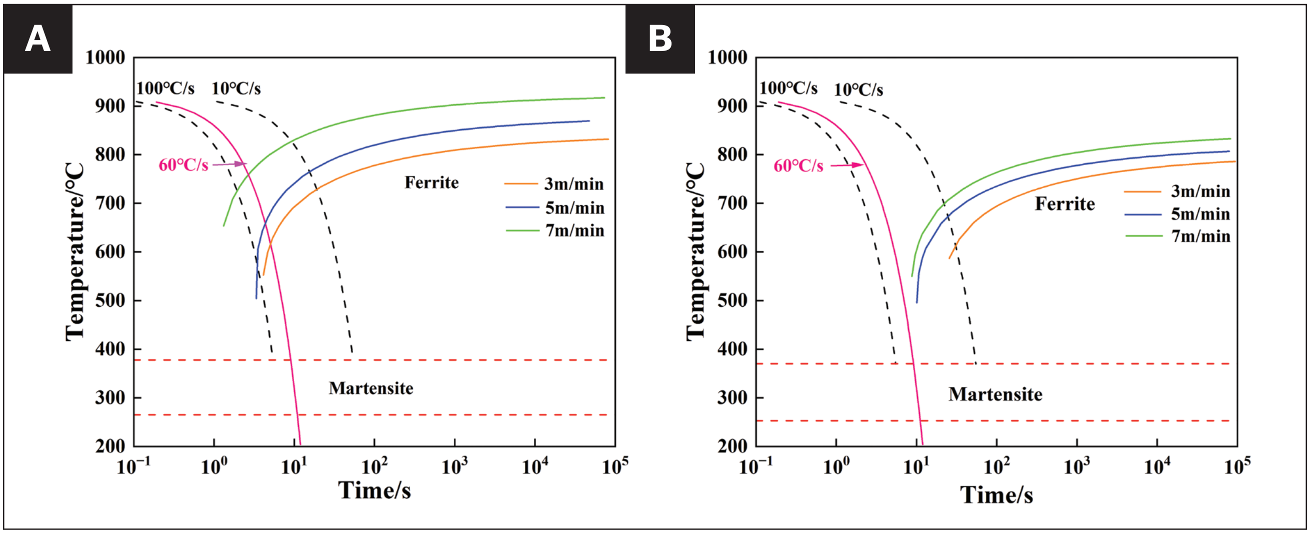

Fig. 7 — Simulated continuous cooling transformation diagrams of welds of PHS: A — Thin coating; B — extra-thin coating.

Table 4 — The Element Contents of the Welds at Different Conditions

No.	Estimated Al Content/ wt-%	Measured Average Al content/wt-%	Estimated C Content/ wt-%	Measured Average C Content/wt-%	Estimated Mn Content/wt-%	Measured Average Mn Content/wt-%
Thin Coating (3 m/min)	0.30	0.24	0.25	0.25	1.03	1.02
Thin Coating (5 m/min)	0.36	0.31	0.24	0.24	1.07	1.07
Thin Coating (7 m/min)	0.41	0.36	0.24	0.24	1.09	1.08
Extra-thin Coating (3 m/min)	0.20	0.17	0.25	0.25	1.04	1.04
Extra-thin Coating (5 m/min)	0.24	0.20	0.25	0.24	1.06	1.05
Extra-thin Coating (7 m/min)	0.29	0.22	0.24	0.24	1.09	1.07

martensite and a small amount of ferrite (Figs. 6A–C). The fraction of ferrite, estimated by Image-Pro Plus software, is shown in Table 3. As the welding speed increased from 3–7 m/min, the ferrite fraction in the thinly coated PHS welds increased from 1.5% to 3%. For the extra-thinly coated PHS, the welds obtained at welding speeds of 3–7 m/min only contained martensite due to further thinning coating (Figs. 6D–F). In contrast, the ferrite fraction in the traditional thickly coated PHS weld was 4.2% if a pure Ni shim was used as a filler metal (Ref. 14). Thus, the ferrite fraction of the welds was significantly reduced by decreasing coating thickness.

In this study, the phase balance in the Al-Si-coated PHS welds was expected to correlate with the element contents. Consequently, the average element contents in the welds were analyzed by EPMA, and the results are listed in Table 4. The measured value of Al content was less than the estimated value because some coating floated on the molten pool surface and did not enter the weld during the short solidification

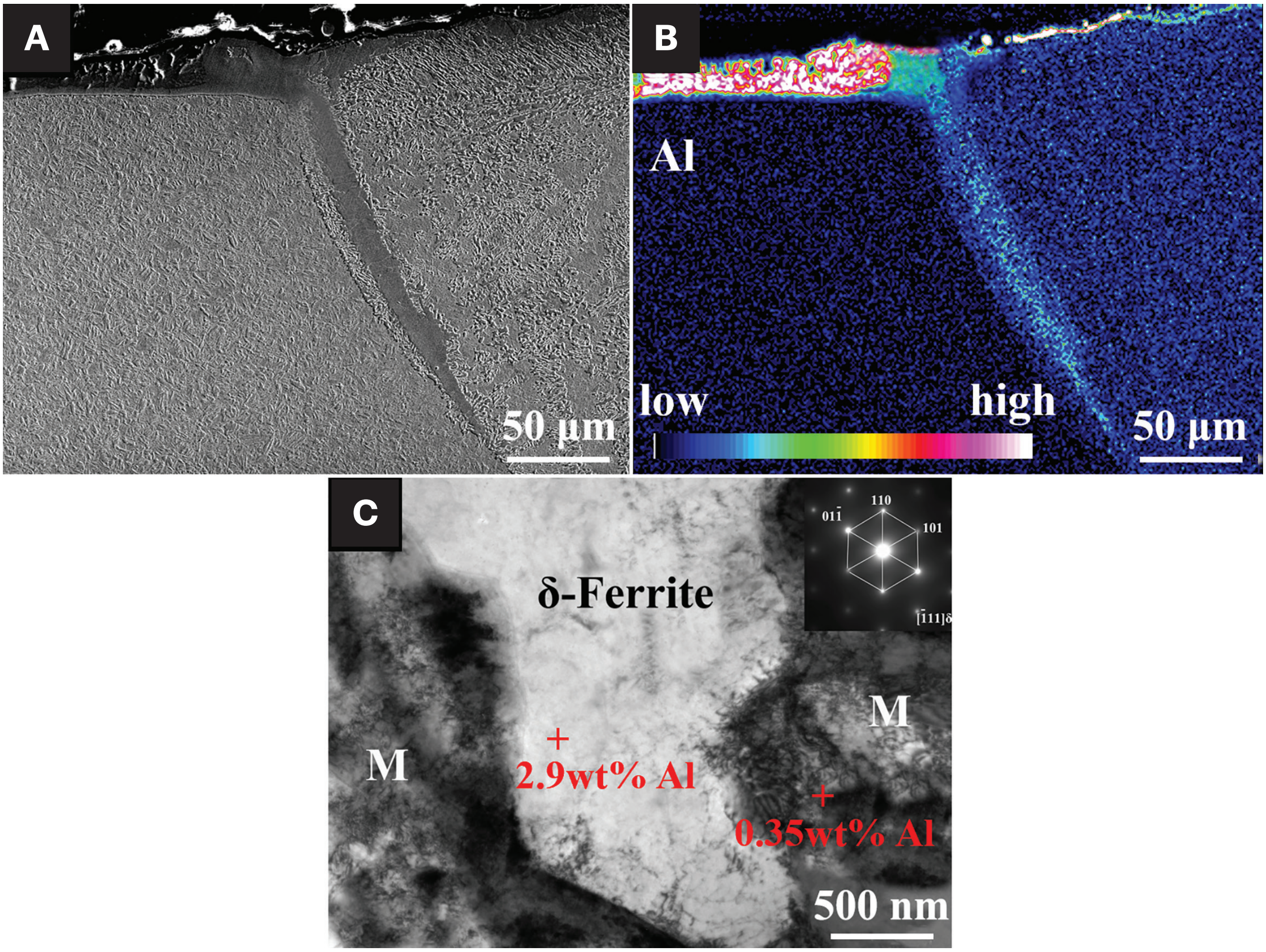

Fig. 8 — A — The SEM image; B — EPMA result of Al distribution; C — TEM image and SAED pattern of the strip-like phase at the weld toe.

process. With an increase in welding speed from 3 m/min to 7 m/min, the Al content in the welds increased from 0.24% to 0.36% for thinly coated PHS and from 0.17% to 0.22% for extra-thinly coated PHS. This variation of Al contents was due to the increased dilution rate as the welding speed increased. The previous study indicated that a higher Al content of 0.9% was achieved in the traditional thickly coated PHS weld by using a filler wire at a welding speed of 3 m/min (Ref. 17). It was clear that the Al content in the Al-Si-coated PHS weld was significantly reduced with thinner coatings. In addition, the measured values of C and Mn contents were almost similar to the estimated values, which indicated that the evaporation loss of elements in the welding process was limited. As the welding speed increased, the average C and Mn contents of the welds slightly decreased, which suggested that the C and Mn elements of the welds had a limited effect on the weld microstructure.

Based on the above analysis, the microstructural evolution in the welds mainly depended on the Al content because the C and Mn content had only a slight variation. The effect of the Al element on the continuous cooling transformations for the welds during press-hardening was simulated by JMatPro software, as shown in Fig. 7. The cooling curves for the press-hardening heat treatments of the thinly coated PHS welds passed through the ferrite and martensite regions, with the ferrite start curves shifting to the left as the welding speed was increased (Fig. 7A). The increased Al content in the weld affected the ferrite transformation kinetics (Ref. 22). Thus, more ferrite was obtained in the thinly coated PHS welds obtained at a higher welding speed. In contrast, the ferrite start curves of the extra-thinly coated PHS welds shifted to the right due to the lower Al contents (Fig. 7B), resulting in full martensite in the extra-thinly coated PHS welds. These simulated results were consistent with the experimental results shown in Fig. 6.

Figure 8 shows the characterization of the strip-like phase obtained at a welding speed of 7 m/min. The strip-like phase forming near the weld toe was distributed along the fusion boundary, which was an Al-enriched region. The Al content was determined by TEM-EDS to be 2.9% (Figs. 8B and C). According to previous reports, when the Al content exceeded 2.7%, δ-ferrite could be retained in the weld after press-hardening (Refs. 23–25). Furthermore, the TEM image with a selected area electron diffraction (SAED) pattern demonstrated that the Al-enriched region consisted of δ-ferrite.

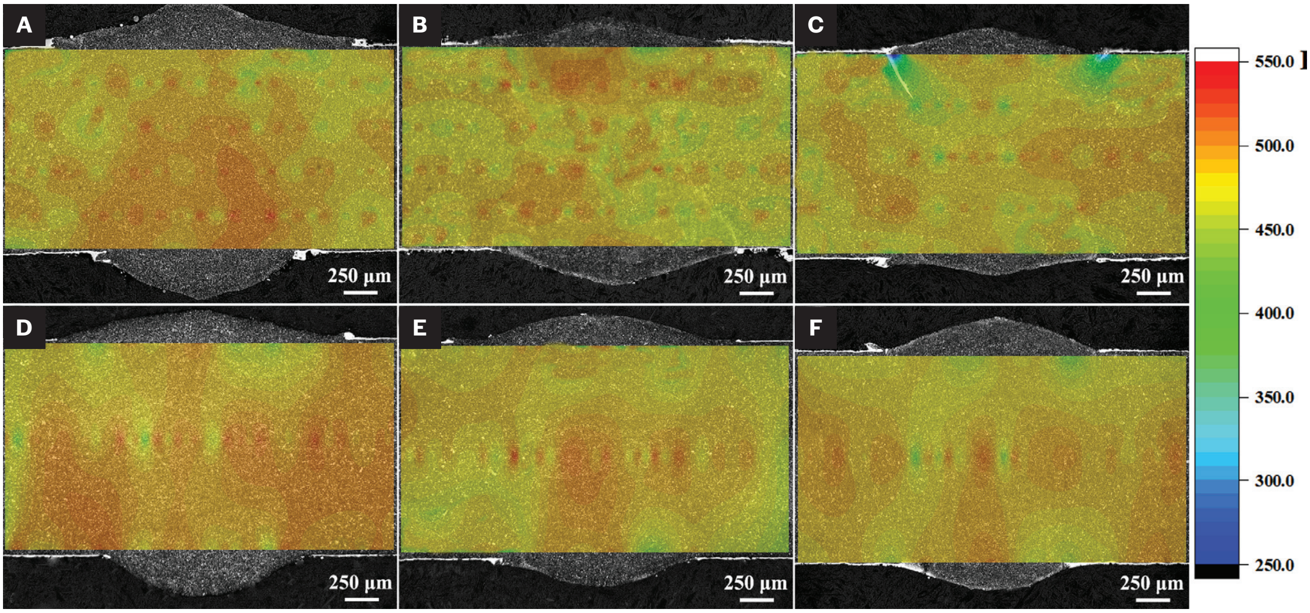

Fig. 9 — Hardness distribution images of joints at different conditions: A–C — Thinly coated PHS; D–F — extra-thinly coated PHS; A and D — 3 m/min; B and E — 5 m/min; C and F — 7 m/min.

Table 5 — Tensile Properties of the Joints at Different Conditions

Samples	Ultimate Tensile Strength/ MPa	Yield Strength/MPa	Total Elongation/%
Thinly Coated PHS	1554 ± 15	1262 ± 13	6.9 ± 0.3
Extra-Thinly Coated PHS	1595 ± 11	1285 ± 15	7.0 ± 0.3
Thinly Coated (3 m/min)	1561 ± 7	1287 ± 17	6.1 ± 0.1
Thinly Coated (5 m/min)	1587 ± 20	1241 ± 16	6.4 ± 0.2
Thinly Coated (7 m/min)	1470 ± 15	1115 ± 10	2.9 ± 0.1
Extra-Thinly Coated (3 m/min)	1552 ± 13	1298 ± 15	5.6 ± 0.2
Extra-Thinly Coated (5 m/min)	1564 ± 5	1260 ± 12	6.1 ± 0.3
Extra-Thinly Coated (7 m/min)	1566 ± 8	1295 ± 17	6.3 ± 0.1

Figure 9 shows the hardness distribution images of the thinly and extra-thinly coated PHS joints. The average hardness of BM was about ~485 HV due to the uniform martensite. The hardness distribution of welds under various conditions was similar, and the average hardness of welds was the same as the BM's. This trend was attributed to the reduction in Al content in the weld, which led to a significant decline in ferrite fraction, thereby increasing overall weld hardness. However, there was a low hardness region at the upper weld toe of the thinly coated PHS joint at a welding speed of 7 m/min, whose hardness was ~375 HV (Fig. 9C). This was attributed to a large amount of ferrite generated by the Al enrichment and ferrite with low hardness (Ref. 25).

Figure 10 shows the engineering stress-strain curves and fracture features of the PHS joints under different conditions, and the tensile properties are listed in Table 5. The thinly coated PHS joints obtained at welding speeds of 3 and 5 m/min failed in the BM. Their ultimate tensile strength (UTS) and yield strength (YS) were comparable to those of the BM,

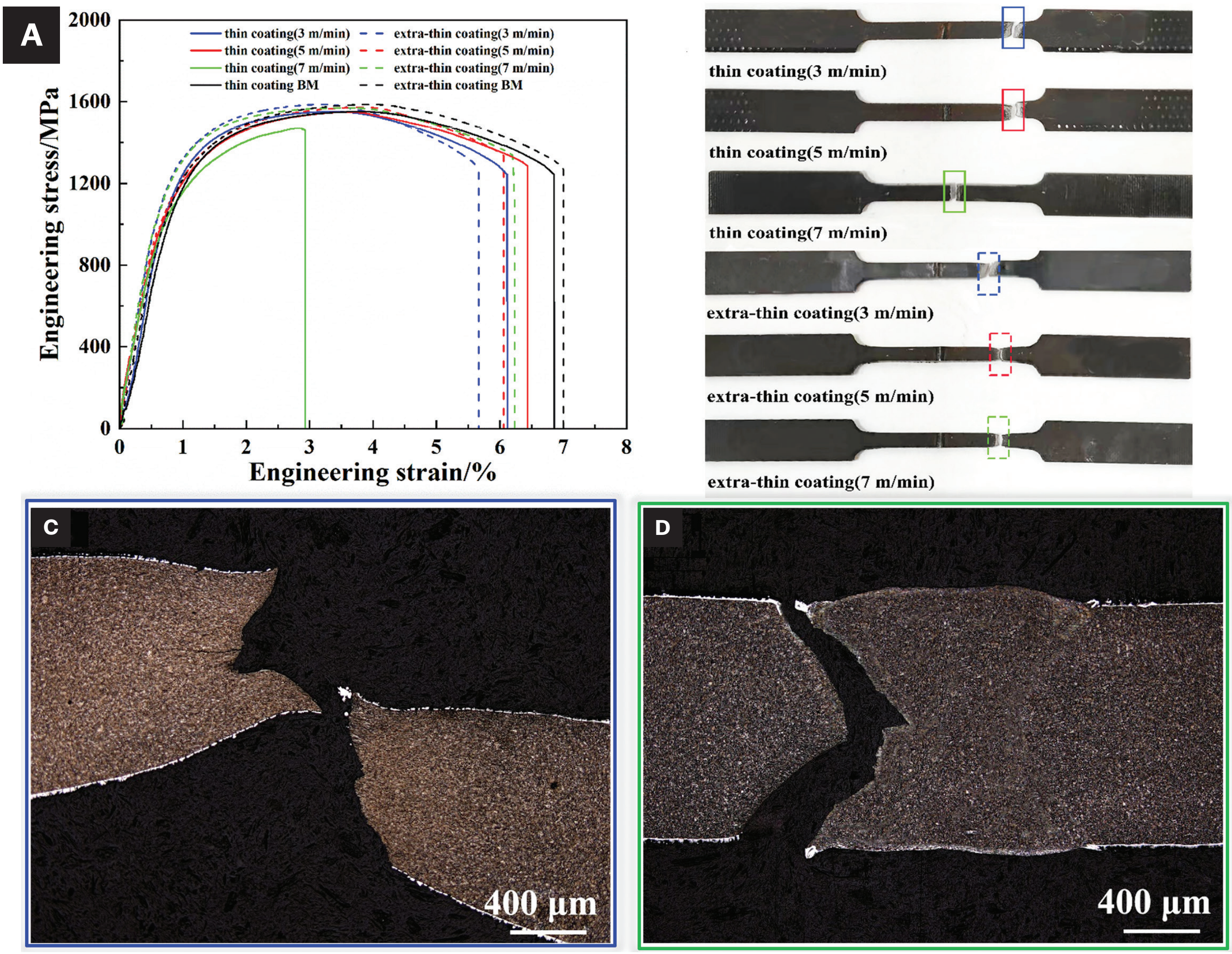

Fig. 10 — A — Engineering stress-strain curves; B–D — tensile fracture locations.

though the total elongation of the joints was slightly lower. However, at a welding speed of 7 m/min, the UTS and YS of the thinly coated PHS joints decreased to 1470 ± 15 and 1115 ± 10 MPa, respectively. Additionally, the elongation dropped to 2.9 ± 0.1%, and the joint fractured at the weld toe, where ferrite was present (Fig. 10D). Conversely, the extra-thinly coated PHS joints obtained at different welding speeds fractured in the BM (Fig. 10B). The UTS and YS of these joints remained comparable to those of the BM, while their elongations were slightly reduced. The results indicated that the tensile properties of the coated PHS joints improved as the coating was thinned. For the Al-Si-coated PHS, the ferrite fraction in the weld was the key factor affecting the mechanical properties, which was significantly decreased by thinning the Al-Si coating and using the filler wire, thereby obtaining welded joints with enhanced properties. However, strip-like ferrite appeared at the weld toe of the thinly coated PHS when the welding speed was 7 m/min. Generally, the soft ferrite presented lower YS and UTS compared to hard martensite (Ref. 26). In this case, cracks tended to initiate at the ferrite/martensite interface and then propagated through the whole weld.

Based on the abovementioned results, the weldability of PHS was improved when using thinner Al-Si coatings. The joints exhibited excellent properties at a wider welding speed range when using a plain C-Mn filler wire. Notably, Al enrichment only appeared with the thinly coated PHS joint obtained at a welding speed of 7 m/min, leading to poor mechanical properties. Some studies have reported that Al enrichment disappeared when the average Al content in the weld dropped below 1.28% (Refs. 5, 21, 27). However, there was a quite low average Al content of 0.36% in the thinly coated PHS weld obtained at a welding speed of 7 m/min, and an obvious strip-like Al enrichment still appeared at the weld toe. The two inconsistent results implied that the formation source of Al enrichment might be unique in the thinly coated PHS welds.

Formation Source of Al Enrichment in Al-Si-Coated PHS Weld Toes

To investigate the Al enrichment formation source in the thinly coated PHS weld, an experiment to selectively remove the coating was designed. It was aimed at the coating on the top surface because the Al-enriched region mainly occurred

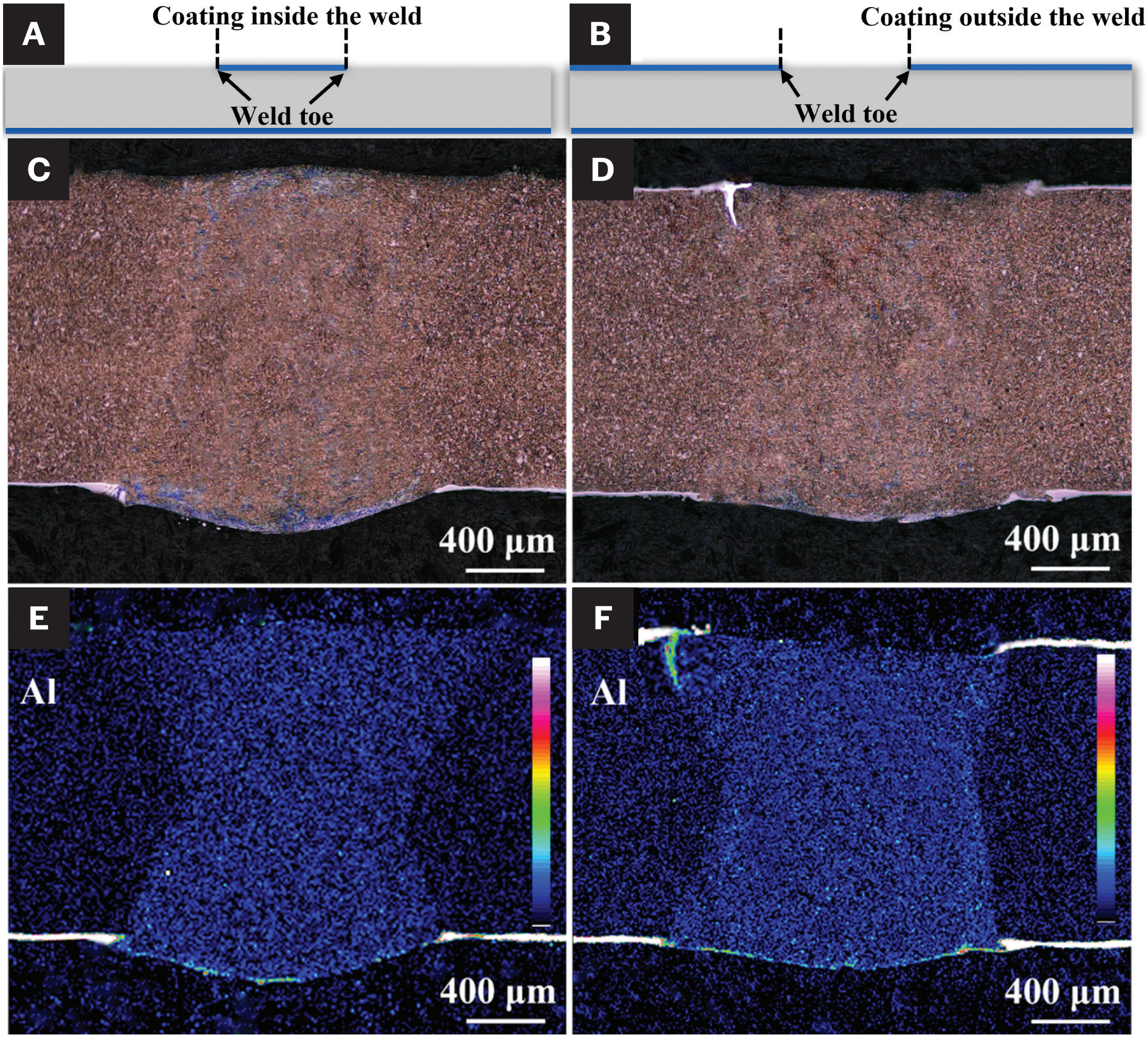

Fig. 11 — A and B — The schematic diagram of selectively removing the coating; C and D — OM images; E and F — Al element distributions of the welds after selectively removing the coating.

at the upper weld toe. In this experiment, two precise weld boundaries were first determined, and then the Al-Si coatings inside and outside the weld were selectively removed by precision machining (Figs. 11A and B). Subsequently, the thinly coated PHS was laser welded at a welding speed of 7 m/min by using a C-Mn wire. After removing the coating outside the weld, no obvious Al enrichment was observed at the weld toe (Figs. 11C and E). However, after removing the coating inside the weld, an obvious stripe-like Al enrichment was observed at the weld toe, and the Al-enriched band was from the coating to the weld toe, showing a continuous feature (Figs. 11D and F). This suggested that the Al enrichment at the weld toe likely originated from the coating outside the weld.

Figures 12A and B show the dynamic behaviors of the molten pools after removing the coating inside the weld. The floating substances in contact with the coating outside the weld were observed at the molten pool boundaries. To determine the chemical compositions of the floating substances, EPMA analysis was carried out; the results are shown in Figs. 12C and D. The floating substances were composition consistent with Al_2O_3, which was the same as the bright islands on the molten pool surface (Fig. 4). The existence of Al_2O_3 indicated that the coating outside the weld intruded the weld when the coating inside the weld had been removed. Therefore, it was determined that the Al enrichment, observed at the thinly coated PHS's weld toe obtained at a welding speed of 7 m/min, was from the coating outside the weld. In addition, the intruded coating occurred at some locations along the length of the weld, which was not consistent across the entire weld length (Fig. 12C). This was related to the stability of the molten pool and keyhole, and a detailed study will be deeply reported in another paper.

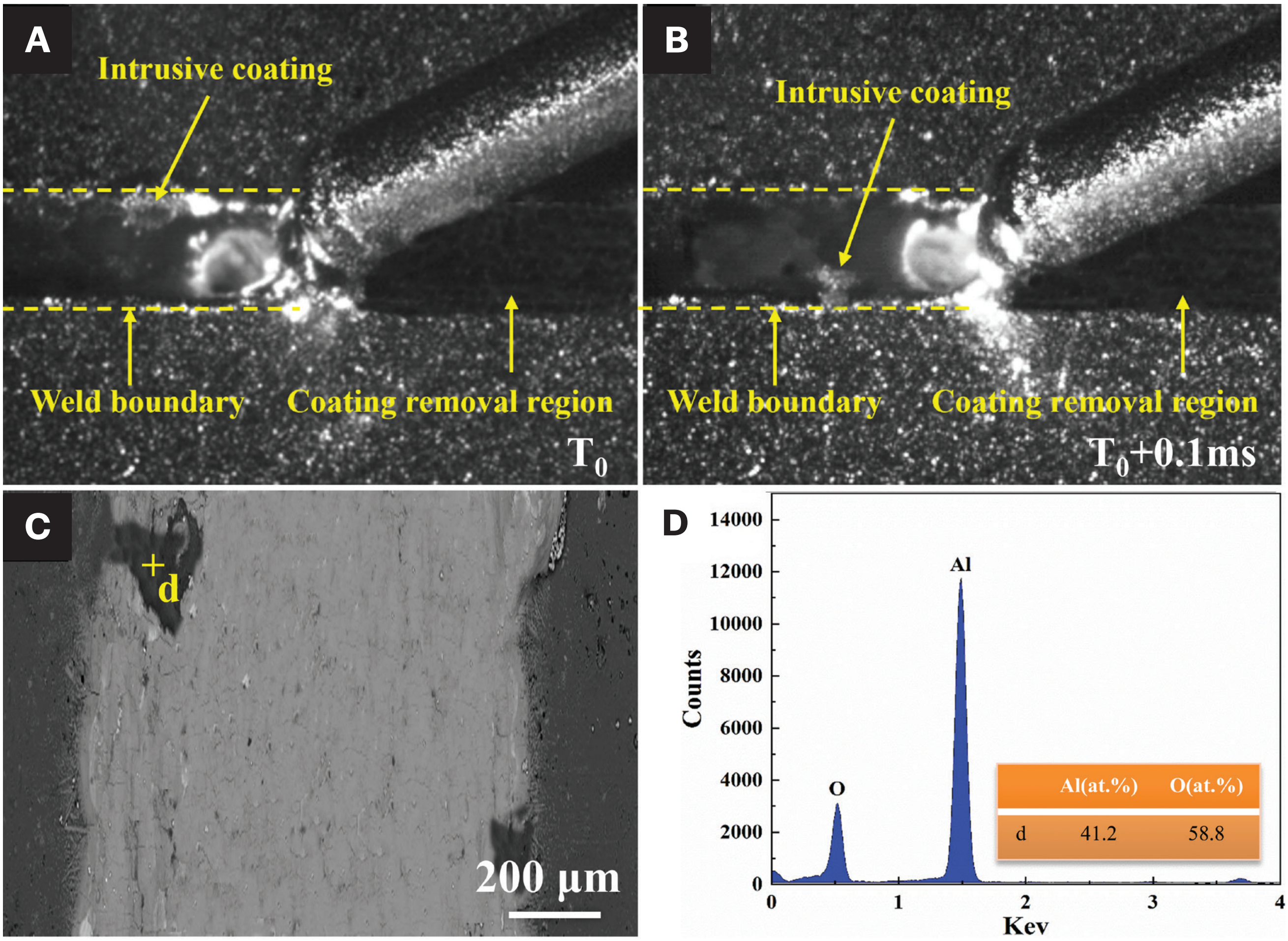

Fig. 12 — A and B — Surface dynamic behaviors of the molten pools; C — backscattered electron image of the weld surface; D — the EPMA result of the floating substance after removing the coating inside the weld.

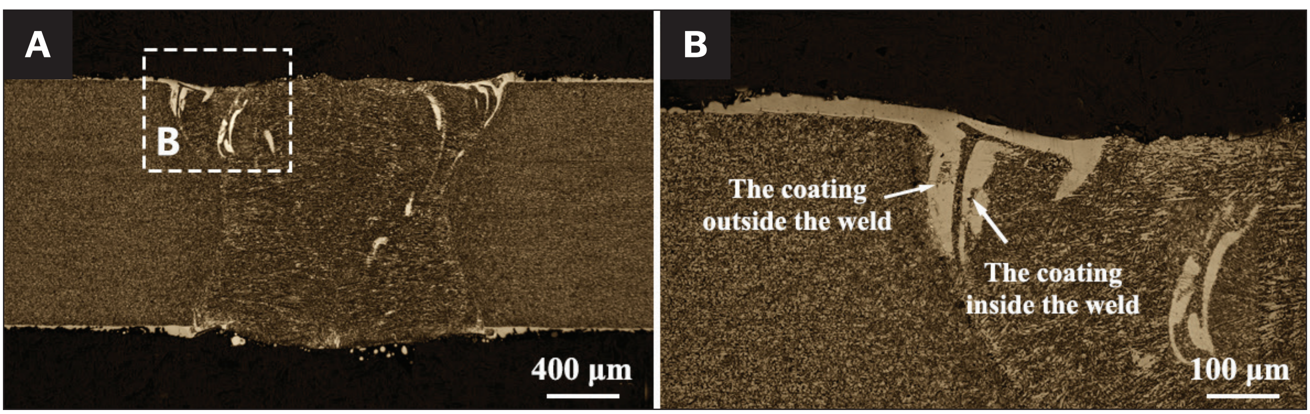

Fig. 13 — A — Macrograph of the thickly coated PHS weld; B — Al enrichment at the weld toe.

The Al intrusion only occurred at the thinly coated PHS's weld toe obtained at a high welding speed of 7 m/min, indicating that the welding speed affected the Al intrusion. Previous studies on laser welding of thickly coated PHS also revealed that the degree of Al intrusion increased as the welding speed increased, but detailed explanations were not provided (Refs. 29, 30). The welding speed could change the heat input, which would affect the overall temperature and flow velocity of the molten pool. At a low welding speed, the temperature and flow velocity of liquid steel were high, which was attributed to the higher heat input at a low welding speed. Thus, the coating at the weld toe could be dragged into the pool and sufficiently diluted. At a high welding speed, the short residence time of the liquid metal resulted in insufficient time for the complete mixing of the invasive coating and retained Al intrusion at the weld toe.

In addition to the thinly coated PHS, there remained a question as to whether similar Al enrichment occurred in conventional thickly coated PHS welds. Consequently, the thickly coated PHS was laser welded, the welding speed was maintained at 7 m/min, and the C-Mn wire was used as filler. Figure 13 shows the Al enrichment in the weld. Significant incomplete mixing of Al was observed in the weld. Notably, some Al-enriched phase contacting with the coating existed at the weld toe, which was determined to come from the coating outside the weld according to the above experimental results. Furthermore, Al enrichment within the weld came from the coating inside because the thick coating could not be effectively diluted. The above results indicated that the two types of Al enrichment simultaneously occurred in the thickly coated PHS weld. In addition, this also suggested that Al intrusion at the weld toe was not unique to thinly coated PHS but is a common problem.

Conclusions

In this study, the laser weldability of PHS with thin and extra-thin Al-Si coatings was evaluated. The metallurgical behaviors and properties of PHS welded joints obtained at different welding speeds were systematically studied. The specific conclusions are as follows:

1. Compared with traditional thickly coated PHS, the weldability of PHS was improved when using thinner Al-Si coatings. Ferrite formation in the weld was significantly inhibited and a wider welding parameters window was obtained. Tensile fractures of thinly coated PHS joints obtained at welding speeds of 3–5 m/min occurred in the BM. For the extra-thinly coated PHS, the joints obtained at welding speeds of 3–7 m/min fractured in the BM. In addition, the requirement of the filler wire was decreased, and only using a plain C-Mn filler wire could inhibit ferrite formation in the weld.

2. Al intrusion occurred at the weld toe with the thin coating obtained at a welding speed of 7 m/min, originating from the coating outside the weld. Al intrusion at the weld toe was related to mixing in the liquid metal, which depended on the welding speed. Al enrichment was difficult to dilute at a high welding speed. The results provided a greater understanding of Al intrusion behavior and provided theoretical guidance for inhibiting this issue.

3. For the conventional thickly coated PHS, Al enrichment was observed at the weld toe and within the weld. The Al-enriched region at the weld toe was in contact with the coating, which came from the coating outside the weld. The Al-enriched region within the weld originated from the coating inside the weld. This observation indicated that Al intrusion at the weld toe was not unique to thinly coated PHS but is a common problem. Moreover, the results provided insight into mitigating Al enrichment in thickly coated PHS welds.

Acknowledgments

This work was supported by the National Nature Science Foundation of China (Nos. 52274378 and 51774085).

References

1. Li, J., Tong, C., Zhang, R., Shi, Z., and Lin, J. 2023. A data-informed review of scientific and technological developments and future trends in hot stamping. *International Journal of Lightweight Materials and Manufacture* 7(2): 327–343. DOI: 10.1016/j.ijlmm.2023.11.003

2. Taylor, T., and Clough, A. 2018. Critical review of automotive hot-stamped sheet steel from an industrial perspective. *Materials Science and Technology* 34(7): 809–861. DOI: 10.1080/02670836.2018.1425239

3. Khan, M. S., Razmpoosh, M. H., Biro, E., and Zhou, Y. 2020. A review on the laser welding of coated 22MnB5 press-hardened steel and its impact on the production of tailor-welded blanks. *Science and Technology of Welding and Joining* 25(6): 447–467. DOI: 10.1080/13621718.2020.1742472

4. Hong, K, M., and Shin, Y. C. 2017. Prospects of laser welding technology in the automotive industry: A review. *Journal of Materials Processing Technology* 245: 46–69. DOI: 10.1016/j.jmatprotec.2017.02.008

5. Yoon, T. J., Oh, M. H., Shin, H. J., and Kang, C. Y. 2017. Comparison of microstructure and phase transformation of laser-welded joints in Al-10wt% Si-coated boron steel before and after hot stamping. *Materials Characterization* 128(7): 195–202. DOI: 10.1016/j.matchar.2017.02.007

6. Saha, D. C., Biro, E., Gerlich, A. P., and Zhou, N. Y. 2016. Fusion zone microstructure evolution of fiber laser welded press-hardened steels. *Scripta Materialia* 121: 18–22. DOI: 10.1016/j.scriptamat.2016.04.032

7. Khan, M. S. 2023. Recent advances in mitigating fusion zone softening during laser welding of Al-Si coated 22MnB5 press-hardened steels. *Materials Research Express.* DOI: 10.1088/2053-1591/acead5

8. Yang, H., Sun, Y., Tan, C., Zhao, X., Chen, B., Song, X., Guo, W., and Feng, J. 2020. Influence of Al-Si coating on microstructure and mechanical properties of fiber laser welded and then press-hardened 22MnB5 steel. *Materials Science and Engineering: A* 794, 139918. DOI: 10.1016/j.msea.2020.139918

9. Chen, X., Zhang, S., Jiang, M., Chen, Y., Jiang, Y., Wang, Z., Jiang, N., Chen, A., Li, B., Lei, Z., and Chen, Y. 2023. Microstructure and mechanical properties of laser welded hot-press-formed steel with varying thicknesses of Al-Si coatings cleaned by nanosecond pulsed laser. *Journal of Materials Research and Technology* 22: 2576–2588. DOI: 10.1016/j.jmrt.2022.12.124

10. Sun, J., Han, Z., Xu, F., Wang, X., Cui, H., and Lu, F. 2020. The segregation control of coating element for pulse fiber laser welding of Al-Si coated 22MnB5 steel. *Journal of Materials Processing Technology* 286: 116833–116844. DOI: 10.1016/j.jmatprotec.2020.116833

11. Xu, W., Tao, W., Luo, H. W., and Yang, S. L. 2023. Effect of oscillation frequency on the mechanical properties and failure behaviors of laser beam welded 22MnB5 weld. *Journal of Materials Research and Technology* 22: 1436–1448. DOI: 10.1016/j.jmrt.2022.12.013

12. Sun, Q., Di, H. S., Wang, X. N., and Chen, X. M. 2019. Suppression of δ-ferrite formation on Al-Si coated press-hardened steel during laser welding. *Materials Letters* 245: 106–109. DOI: 10.1016/j.matlet.2019.02.111

13. Chen, X. M, Wang, X. N, Sun, Q., Hu, Z., Huan, P. C., Yi, G., Hiromi, N., Di, H. S., and Sun, L. 2020. Improving the mechanical properties of PHS laser welded joints by adding Ni foil to suppress δ-ferrite. *Journal of Materials Research and Technology* 9: 5184–5193. DOI: 10.1016/j.jmrt.2020.03.035

14. Khan, M. S., Macwan, A., Biro, E., and Zhou, Y. 2021. α-Ferrite suppression during fiber laser welding of Al-Si coated 22MnB5 press-hardened steel. *Welding Journal* 100(6): 213-s to 220-s.

15. Anderson, H., Malmberg, N., and Garnick, P. Method for joining two blanks. C.N. Patent 106488824 A.

16. Coviello, D., von der Heydt, J., Rullo, L., Keßler, M., De Vito, M., D'Angola, A., and Sorgente, D. 2023. Laser welding of tailored blanks made of Al-Si-coated 22MnB5 steel using a filler wire and variable energy distribution laser optics. *The International Journal of Advanced Manufacturing Technology* 125(5): 2691–2704. DOI: 10.1007/s00170-023-10921-4

17. Xu, W., Jiang, Z., Zhang, J., Tao, W., Zhang, X., and Yang, S L. 2023. Direct laser-filler wire welding of Al-Si coated 22MnB5 steel without removing the Al-Si coating. *Journal of Materials Research and Technology* 24: 2265–2278. DOI: 10.1016/j.jmrt.2023.03.138

18. Yi, H. L., Chang, Z. Y., Liu, Z. Y., Yang, D. P., and Xiong, X. C. Hot stamping and forming components, pre-painted steel sheets for hot stamping and forming, and hot stamping and forming processes. C.N. Patent 108588612 A.

19. Wang, Z., Cao, Z. H., Wang, J. F., and Huang, M. X. 2021. Improving the bending toughness of Al-Si coated press-hardened steel by tailoring coating thickness. *Scripta Materialia* 192(3): 19–25. DOI: 10.1016/j.scriptamat.2020.10.008

20. Chen, N., Wan, Z., Wang, H. P., Li, J., Solomon, J., and Carlson, B. E. 2020. Effect of Al-Si coating on laser spot welding of press hardened steel and process improvement with annular stirring. *Materials & Design* 195: 108986. DOI: 10.1016/j.matdes.2020.108986

21. Lin, W. H., Li, F., Hua, X. M., and Wu, D. S. 2018. Effect of filler wire on laser welded blanks of Al-Si-coated 22MnB5 steel. *Journal of Materials Processing Technology* 259: 195–205. DOI: 10.1016/j.jmatprotec.2018.04.041

22. Bhattacharya, A., Bokinala, P. K., Mitra, R., and Chakrabarti, D. 2019. Relative effect of C and Mn on strength-toughness of medium Mn steels. *Materials Science and Technology* 35: 56–67. DOI: 10.1080/02670836.2018.1537609

23. Guo, S., Jin, Z.Q., Liu, Y.Q., Wang, F.R., Wang, Y.Q., Li, Z.X., Yi, H.L., and Xie, G.M. 2024. Achieving excellent properties of laser tailor-welded thin Al-Si coated press-hardened steel joint via controlling dilution rate. *Journal of Manufacturing Processes* 131: 879–890. DOI: 10.1016/j.jmapro.2024.09.065

24. Ding, K., Wu, T., Dong, W., Hu, T., Li, S., Zhu, P., Sun, Y., Zhou, J., Pan, H., and Gao, Y. 2023. Clarification of the ferrite formed in the laser welded joint of the Al-Si coated press-hardened steel. *Journal of Materials Research and Technology* 23: 5880–5891. DOI: 10.1016/j.jmrt.2023.02.185

25. Wang, X. N., Yi, G., Sun, Q., Xiao, M., Gao, Y., Zhang, Z. H., Di, H. S., and Zhou, Y. N. 2020. Study on δ-ferrite evolution and properties of laser fusion zone during post-weld heat treatment on Al-Si coated press-hardened steel. *Journal of Materials Research and Technology* 9: 5712–5722. DOI: 10.1016/j.jmrt.2020.03.096

26. Yang, D. P., Du, P. J., Wu, D. and Yi, H. L. 2021. The microstructure evolution and tensile properties of medium-Mn steel heat-treated by a two-step annealing process. *Journal of Materials Science & Technology* 75: 205–215. DOI: 10.1016/j.jmst.2020.10.032

27. Xu, W., Tao, W., Luo, H., and Yang, S. L. 2022. Effect of welding speed on microstructure and mechanical behavior of laser welded Al-Si coated 22MnB5 steel. *Optics & Laser Technology* 154: 108344. DOI: 10.1016/j.optlastec.2022.108344

28. Khan, M. S., Shahabad, S. I., Yavuz, M., Duley, W. W., Biro, E., and Zhou, Y. 2021. Numerical modeling and experimental validation of the effect of laser beam defocusing on process optimization during fiber laser welding of automotive press-hardened steels. *Journal of Manufacturing Processes* 67: 535–544. DOI: 10.1016/j.jmapro.2021.05.006.

29. Saha, D. C., Biro, E., Gerlich, A. P., and Zhou, Y. N. 2016. Fiber laser welding of Al-Si coated press-hardened steel. *Welding Journal* 95(5): 147-s to 156-s.

30. Kang, M., Kim, Y. M., and Kim, C. 2016. Effect of heating parameters on laser welded tailored blanks of hot press forming steel. *Journal of Materials Processing Technology* 228: 137–144. DOI: 10.1016/j.jmatprotec.2015.06.028

ZHIQI JIN, **SHENG GUO**, **ZHIYONG ZHANG**, **YUQIAN WANG**, **GUANGMING XIE** (*xiegm@ral.neu.edu.cn*), **ZHENGXIAN LI** and **HONGLIANG YI** are with State Key Laboratory of Rolling and Automation, Northeastern University, Shenyang, China. **LI** and **YI** are also with Easyforming Materials Technology Co., Ltd., Suzhou, China.